TU Delft

Delft University of Technology

# Viscoelastic Tides of Mercury and the Determination of its Inner Core Size

Steinbrügge, G.; Padovan, S.; Hussmann, H.; Steinke, T.; Stark, A.; Oberst, J.

**DOI**
10.1029/2018JE005569

**Publication date**
2018

**Document Version**
Final published version

**Published in**
JRG Planets

**Citation (APA)**
Steinbrügge, G., Padovan, S., Hussmann, H., Steinke, T., Stark, A., & Oberst, J. (2018). Viscoelastic Tides of Mercury and the Determination of its Inner Core Size. *JRG Planets*, *123*(10), 2760-2772. https://doi.org/10.1029/2018JE005569

**Important note**
To cite this publication, please use the final published version (if applicable).
Please check the document version above.

**Copyright**
Other than for strictly personal use, it is not permitted to download, forward or distribute the text or part of it, without the consent of the author(s) and/or copyright holder(s), unless the work is under an open content license such as Creative Commons.

**Takedown policy**
Please contact us and provide details if you believe this document breaches copyrights.
We will remove access to the work immediately and investigate your claim.

*This work is downloaded from Delft University of Technology.*
*For technical reasons the number of authors shown on this cover page is limited to a maximum of 10.*

Journal of Geophysical Research: Planets

RESEARCH ARTICLE
10.1029/2018JE005569

# Viscoelastic Tides of Mercury and the Determination of its Inner Core Size

G. Steinbrügge[1,2], S. Padovan[1], H. Hussmann[1], T. Steinke[3], A. Stark[1], and J. Oberst[1]

[1]German Aerospace Center (DLR), Institute of Planetary Research, Berlin, Germany, [2]Institute for Geophysics, University of Texas at Austin, Austin, TX, USA, [3]Delft University of Technology, Delft, The Netherlands

**Key Points:**
- We predict Mercury's tidal Love number $h_2$ to be in the range from 0.77 to 0.93 based on interior models compliant with MESSENGER results
- The ratio $h_2/k_2$ may constrain the size of the inner core, provided it responds elastically to the solar tide
- Using an Andrade rheology Mercury's phase-lag is estimated to be 4° at maximum corresponding to a surface heat flux smaller than 0.16 mW/m$^2$

**Supporting Information:**
- Data Set S1
- Figure S1

**Correspondence to:**
G. Steinbrügge,
gregor.steinbruegge@dlr.de

**Citation:**
Steinbrügge, G., Padovan, S., Hussmann, H., Steinke, T., Stark, A., & Oberst, J. (2018). Viscoelastic tides of Mercury and the determination of its inner core size. *Journal of Geophysical Research: Planets*, *123*, 2760–2772. https://doi.org/10.1029/2018JE005569

Received 7 FEB 2018
Accepted 1 SEP 2018
Accepted article online 9 SEP 2018
Published online 23 OCT 2018

©2018. American Geophysical Union. All Rights Reserved.

**Abstract** We computed interior structure models of Mercury and analyzed their viscoelastic tidal response. The models are consistent with MErcury Surface, Space Environment, GEochemistry, and Ranging mission inferences of mean density, mean moment of inertia, moment of inertia of mantle and crust, and tidal Love number $k_2$. Based on these constraints we predict the tidal Love number $h_2$ to be in the range from 0.77 to 0.93. Using an Andrade rheology for the mantle the tidal phase-lag is predicted to be 4° at maximum. The corresponding tidal dissipation in Mercury's silicate mantle induces a surface heat flux smaller than 0.16 mW/m$^2$. We show that, independent of the adopted mantle rheological model, the ratio of the tidal Love numbers $h_2$ and $k_2$ provides a better constraint on the maximum inner core size with respect to other geodetic parameters (e.g., libration amplitude or a single Love number), provided it responds elastically to the solar tide. For inner cores larger than 700 km, and with the expected determination of $h_2$ from the upcoming BepiColombo mission, it may be possible to constrain the size of the inner core. The measurement of the tidal phase-lag with an accuracy better than ≈0.5° would further allow constraining the temperature at the core-mantle boundary for a given grain size and therefore improve our understanding of the physical structure of Mercury's core.

**Plain Language Summary** Due to the proximity to the Sun, tides are raised on Mercury in a similar way the Moon causes ocean tides on Earth. Although Mercury's surface is rigid, a large fluid core causes a tidal wave propagating around the planet. Using results from NASA's MESSENGER mission, we calculate that the surface should also deform by around 20 cm to 2.40 m during each Mercury orbit around the Sun. This is an amplitude that could be detected with a laser altimeter, one of the instruments onboard the upcoming BepiColombo mission. We show how the interior structure of the planet, in particular the size of an inner solid core, can be constrained by the tidal measurement. This result will help us to better understand Mercury's evolution and to constrain models explaining the magnetic field generation in Mercury's iron core.

## 1. Introduction

From 2011 to 2015, NASA's MErcury Surface, Space Environment, GEochemistry, and Ranging (MESSENGER) spacecraft (Solomon et al., 2011) orbited Mercury and was able to provide, in combination with Earth-based radar measurements, a set of geodetic constraints on the interior structure of the planet. Mercury's mean radius of (2,439.36 ± 0.02) km (Perry et al., 2015) in combination with the gravitational parameter $GM$ of (2.203209 ± 0.000091) ×10$^{13}$ m/s$^2$ (Verma & Margot, 2016) leads to a mean density of 5,427.75 kg/m$^3$. This high value in combination with Mercury's size indicates a significant fraction of iron in Mercury's composition. The mean moment of inertia (MoI) has been first determined by ground-based radar observations of Mercury's spin state to a value of $C/MR^2 = 0.346 \pm 0.014$ (Margot et al., 2007). With updated values for the gravity field inferred from MESSENGER radio science observations, a value of 0.349 ± 0.014 was found (Mazarico et al., 2014). The measurement of the physical librations at the 88 days orbital period using laser altimetry and stereo imaging data gave a value of 0.343 ± 0.014 (Baland et al., 2017; Stark et al., 2015). A value smaller than 0.4 indicates a concentration of mass toward the center of the planet, thus indicating the abundant iron is likely concentrated in a large core. In the Cassini state, a combination of libration amplitudes, gravitational field, and obliquity provides an estimate of the MoI of the mantle and crust (Peale, 1976; Peale et al., 2002). The determined values for the fractional part of the MoI of the mantle and crust ($C_m/C$) range between 0.431 ± 0.025 (Margot et al., 2012) and 0.421 ± 0.021 (Stark et al., 2015). The measured libration amplitudes of (35.8 ± 2) arc

seconds (Margot et al., 2007) and (38.9 ± 1.3) arc seconds (Stark et al., 2015) reveal an at least partially molten core (Hauck et al., 2013; Margot et al., 2007, 2012; Stark et al., 2015). Further constraints come from the measurement of Mercury's tidal Love number $k_2$. The value indicates the added contribution to an imposed unit amplitude gravity potential of degree 2 at the surface of the planet due to an internal redistribution of mass. This redistribution is a consequence of the tidal forcing that is exerted by the Sun during Mercury's orbit. $k_2$ has been determined to be 0.451 ± 0.014 by Mazarico et al. (2014) and 0.464 ± 0.023 by Verma and Margot (2016). Based on the $k_2$ determination of Mazarico et al. (2014), Padovan et al. (2014) examined multiple interior models in agreement with the $k_2$ measurement. The authors showed that in the presence of a liquid core with known size, $k_2$ is informative of the temperature and rheological parameters of the mantle. They inferred a cold and/or rigid mantle and further concluded that the presence of a previously suggested solid FeS layer (Malavergne et al., 2010; Smith et al., 2012) is only in agreement with the measurements when the temperature at the core-mantle boundary (CMB) is <1,600 K.

The core generates a weak magnetic field with an unusually large quadropole moment (Anderson et al., 2012). Possible origins are the classical dynamo driven by latent heat and chemically induced density differences from crystallization at the inner core boundary (Cao et al., 2014; Manglik et al., 2010), but alternative models involving iron snow formation dynamics have been proposed (Dumberry & Rivoldini, 2015). Independent of the model assumed, a key factor of the magnetic field generation models is the presence and, if it exists, the size of the solid inner core.

Since a solid core has a different density than a liquid core in the presence of light-alloying elements, the density contrast also influences the polar MoI. The mantle MoI indirectly depends on the inner core, since the core and mantle MoI needs to sum up to the polar MoI. However, the different MoIs do not give unique solutions for the currently published values, thus, it is not possible to determine the inner core size from these quantities (Rivoldini & Van Hoolst, 2013). In this work we study the tidal deformation of Mercury based on the geodetic constraints from the MESSENGER mission and show that a future determination of the tidal Love number $h_2$ can yield important constraints on the inner core size, when combined with the available (or future) measurements of $k_2$. We further study the potential range of tidal phase-lags and resulting tidal heat dissipation in Mercury's mantle. All the geodetic parameters discussed in this paper are expected to be measured by the upcoming BepiColombo mission (Benkhoff et al., 2010) scheduled for launch in October 2018 and operated by the European Space Agency and the Japan Aerospace Exploration Agency.

## 2. Methods

The construction of the interior models of Mercury follows a two-step approach. We first compute structural models, which are then used to compute the tidal response of the planet. The interior models consist of three chemically separated layers: a core surrounded by a mantle and a crust. While the crust is kept as one single layer, the mantle and core are further subdivided into 5 and 20 equally spaced sublayers, respectively. Each sublayer is characterized by its thickness, density, temperature, pressure, viscosity, and rigidity. We tested that a larger number of sublayers would not affect the results.

### 2.1. Governing Equations

The models are built from outside to inside and generally follow the recipe from previous studies (e.g., Hauck et al., 2007, 2013; Knibbe & van Westrenen, 2015). Assuming the densities in the mantle and crust to be constant, we compute the pressure and gravitational acceleration at the CMB. From there on, pressure and temperature of the core are propagated inward satisfying equations (1)–(5). Equation (1) is a third-order Birch-Murnaghan equation of state giving the pressure $P$ at radius $r$ as a function of density $\rho$ and temperature $T$.

$$P(r) = \frac{3K_0}{2}\left[\left(\frac{\rho}{\rho_0}\right)^{7/3} - \left(\frac{\rho}{\rho_0}\right)^{5/3}\right] \cdot \left[1 + \frac{3}{4}(K_0' - 4)\left(\left(\frac{\rho}{\rho_0}\right)^{2/3} - 1\right)\right] + \alpha_0 K_0 (T(r) - T_0). \quad (1)$$

$T_0$, $\rho_0$, $K_0$, $K_0'$, and $\alpha_0$ are the reference temperature, density, isothermal bulk modulus as well as its pressure derivative, and the reference volumetric coefficient of thermal expansion, respectively. A list of all parameters used to calculate the properties of the core in this study can be found in Table 1.

**Table 1**
*Parameters Derived From Laboratory Measurements Used for the Computation of the Interior Structure of Mercury's Liquid and Solid Core*

| **Solid Core** | | | |
|---|---|---|---|
| **Parameter** | **Value** | **Unit** | **Source** |
| $T_{0,Fe}$ | 298 | K | Komabayashi and Fei (2010) |
| $\rho_{0,Fe}$ | 8,170 | kg/m$^3$ | Komabayashi and Fei (2010) |
| $K_{0,Fe}$ | 165.3 | GPa | Komabayashi and Fei (2010) |
| $K'_{0,Fe}$ | 5.5 | - | Komabayashi and Fei (2010) |
| $\alpha_{0,Fe}$ | $6.4 \times 10^{-5}$ | K$^{-1}$ | Komabayashi and Fei (2010) |
| $T_{0,Fe\text{-}Si\ (17\ wt\%)}$ | 300 | K | Lin et al. (2003) |
| $\rho_{0,Fe\text{-}Si\ (17\ wt\%)}$ | 7,147 | kg/m$^3$ | Lin et al. (2003) |
| $K_{0,Fe\text{-}Si\ (17\ wt\%)}$ | 141 | GPa | Lin et al. (2003) |
| $K'_{0,Fe\text{-}Si\ (17\ wt\%)}$ | 5.7 | - | Lin et al. (2003) |
| $\alpha_{0,Fe\text{-}Si\ (17\ wt\%)}$ | $5.5 \times 10^{-5}$ | K$^{-1}$ | Uchida et al. (2001), Lin et al. (2003) |
| **Liquid Core** | | | |
| **Parameter** | **Value** | **Unit** | **Reference** |
| $T_{0,Fe\text{-}Si\ (17\ wt\%)}$ | 1650 | K | Sanloup et al. (2004) |
| $\rho_{0,Fe\text{-}Si\ (17\ wt\%)}$ | 6,300 | kg/m$^3$ | Sanloup et al. (2004) |
| $K_{0,Fe\text{-}Si\ (17\ wt\%)}$ | 79 | GPa | Sanloup et al. (2004) |
| $K'_{0,Fe\text{-}Si\ (17\ wt\%)}$ | 4 | - | Sanloup et al. (2004) |
| $\alpha_{0,Fe\text{-}Si\ (17\ wt\%)}$ | $9.2 \times 10^{-5}$ | K$^{-1}$ | Sanloup et al. (2004) |
| $T_{0,FeS}$ | 1770 | K | Knibbe and van Westrenen (2015) and Sanloup et al. (2000) |
| $\rho_{0,FeS,a}$ | 31,524 | kg/m$^3$ | Knibbe and van Westrenen (2015),Sanloup et al. (2000), and Jing et al. (2014) |
| $\rho_{0,FeS,b}$ | −20,012 | kg/m$^3$ | Knibbe and van Westrenen (2015),Sanloup et al. (2000), and Jing et al. (2014) |
| $\rho_{0,FeS,c}$ | 7,019 | kg/m$^3$ | Knibbe and van Westrenen (2015),Sanloup et al. (2000), and Jing et al. (2014) |
| $K_{0,FeS,a}$ | 780.8 | GPa | Knibbe and van Westrenen (2015),Sanloup et al. (2000), and Jing et al. (2014) |
| $K_{0,FeS,b}$ | −462.4 | GPa | Knibbe and van Westrenen (2015),Sanloup et al. (2000), and Jing et al. (2014) |
| $K_{0,FeS,c}$ | 86.6 | GPa | Knibbe and van Westrenen (2015),Sanloup et al. (2000), and Jing et al. (2014) |
| $K'_{0,FeS}$ | 5.1 | - | Knibbe and van Westrenen (2015),Sanloup et al. (2000), and Jing et al. (2014) |
| $\alpha_{0,FeS}$ | $9.2 \times 10^{-5}$ | K$^{-1}$ | Knibbe and van Westrenen (2015),Sanloup et al. (2000), and Jing et al. (2014) |

*Note.* The hyphen indicates that the respective quantity is unitless.

The pressure can be calculated from the overlaying layers by integrating from the outer radius $R$ down to the current radius $r$:

$$P(r) = \int_R^r \rho(x) g(x) dx, \tag{2}$$

where the function $g$ denotes the gravitational acceleration of each layer and can be calculated by

$$g(r) = \frac{4\pi G}{r^2} \int_0^r \rho(x) x^2 dx. \tag{3}$$

The adiabatic temperature profile in the core is obtained by integration of the adiabatic relation

$$\frac{dT}{dP} = \frac{\alpha T}{\rho C_p}, \tag{4}$$

where $C_p$ is the thermal and $\alpha$ is the thermal expansion coefficient. If the temperature is above the Debye temperature, which is around 1000 K for terrestrial planets, the thermal expansion coefficient can be obtained from

$$\alpha_0 K_0 = \alpha \rho \frac{dP}{d\rho}. \tag{5}$$

In this work we use a thermal heat capacity for the core of 825 J/(kg K) (Beutl et al., 1994; Knibbe & van Westrenen, 2015). We use a constant heat capacity within our models, but variations of this value have little

influence on our results. By performing the inward propagation, the problem reduces to solving equations (1), (4), and (5). These are solved simultaneously for the density $\rho$ at the given depth, the temperature $T$, and the coefficient of thermal expansion $\alpha$ using a Levenberg-Marquardt algorithm (Levenberg, 1944; Marquardt, 1963) to allow for self-consistent core models. For models with mixed Fe-FeS-FeSi composition, the parameters in equations (1)–(5) are linearly interpolated from the values given in Table 1. The bulk modulus of sulfur is quadratically interpolated as

$$K_{0,\mathrm{FeS}} = K_{0,\mathrm{FeS},a} \cdot \chi_S^2 + K_{0,\mathrm{FeS},b} \cdot \chi_S + K_{0,\mathrm{FeS},c}^2. \tag{6}$$

At each sublayer the liquidus for the respective sulfur and silicon content is checked and if the temperature is lower than the melting temperature at the corresponding pressure, the state of the core below and including that sublayer is switched from liquid to solid. The parameterization for the liquidus of a sulfur-enriched Fe core is taken from Dumberry and Rivoldini (2015) and modified according to Knibbe and van Westrenen (2015) to account for the further decrease of the melting temperature due to the Si content. The melting temperature of the Fe-FeS-FeSi system is then described as a function of pressure $P$, sulfur content $\chi_S$, and silicon content $\chi_{\mathrm{Si}}$ as

$$T_m(P, \chi_S, \chi_{\mathrm{Si}}) = T_{m,\mathrm{Fe}}(P) - \frac{T_{m,\mathrm{Fe}}(P) - T_{e_S}(P)}{\chi_{e_S}} \chi_S - \frac{T_{m,\mathrm{Fe}}(P) - T_{e_{\mathrm{Si}}}(P)}{\chi_{e_{\mathrm{Si}}}} \chi_{\mathrm{Si}}. \tag{7}$$

$T_{m,\mathrm{Fe}}$ is the melting temperature of pure iron which is parameterized as a function of pressure by

$$T_{m,\mathrm{Fe}}(P) = a_1 (P_0 + P)^{a_2}, \tag{8}$$

with $a_1 = 495.5$ K/GPa$^{a2}$, $a_2 = 0.42$, and $P_0 = 22.2$ GPa (Dumberry & Rivoldini, 2015). In equation (7), $T_{e_S}$ and $T_{e_{\mathrm{Si}}}$ are the eutectic temperatures of the FeS system with sulfur content $\chi_{e_S}$ and the FeSi system with the silicon content $\chi_{e_{\mathrm{Si}}}$, respectively. The FeS system is parameterized as a function of pressure as

$$T_{e_S}(P) = \begin{cases} 1265\mathrm{K} - 11.15(P - 3\mathrm{GPa})\mathrm{K/GPa} & \text{for } 3 \text{ GPa} \leq \mathrm{P} < 14 \text{ GPa} \\ 1143\mathrm{K} - 29(P - 14\mathrm{GPa})\mathrm{K/GPa} & \text{for } 14 \text{ GPa} \leq \mathrm{P} < 21 \text{ GPa} \\ 1346\mathrm{K} - 13(P - 21\mathrm{GPa})\mathrm{K/GPa} & \text{for } 21 \text{ GPa} \leq \mathrm{P} < 60 \text{ GPa} \end{cases} \tag{9}$$

and

$$\chi_{e_S} = 0.11 + 0.187 \exp\left(-\frac{0.065P}{\mathrm{GPa}}\right). \tag{10}$$

Since no information about the eutectic temperature of FeSi as a function of pressure is available from experimental data, we follow the approach of Knibbe and van Westrenen (2015) and use $T_{m,\mathrm{Fe}}(P) - T_{e_{\mathrm{Si}}} = 400$ K at 26 wt% Si based on the lab measurements from Kuwayama and Hirose (2004).

The inner core is assumed to be isothermal and to have an FeSi alloy composition with a silicon content being the same as in the liquid phase. Once the melting point is crossed, we keep the temperature below that point isothermal in our model. For sulfur contents up to 15 wt%, sulfur does not solidify and stays in the liquid phase leading to a sulfur free inner core, for higher contents an additional FeS layer would form. In the presence of silicon it has also been suggested that the liquid core would partition into a lower Si-rich part and an upper S-rich part leading to an accretion of solid FeS in the mantle layer (Hauck et al., 2013). However, previous studies (Knibbe & van Westrenen, 2015; Padovan et al., 2014) seem to indicate that the presence of such layer is unlikely, and therefore this particular case is not further treated in this study. Additionally, there are possible regimes in which the melting point curve can be crossed in the upper part of the core generating iron snow (Dumberry & Rivoldini, 2015). We do not consider this possibility since the goal of this work is to investigate the effect of an inner core on the geodetic parameters, not to constrain the inner core composition or growth mechanism. We obtain inner core sizes encompassing previously published ranges (section 3).

### 2.2. Structural Models

Typically, interior structure models are built using either standard Monte-Carlo methods (e.g., Hauck et al., 2013; Knibbe & van Westrenen, 2015) or Bayesian methods (e.g., Rivoldini & Van Hoolst, 2013). Here we approach the modeling in a slightly different way. We first create grids both for the input parameters (crustal density and thickness, and sulfur and silicon content in the core, CMB temperature) and for the observables

(mean density, polar MoI, and MoI of the mantle and crust). The initial crust parameters are varied between thicknesses of 10 and 40 km with a step size of 2 km and densities between 2,600 and 4,000 kg/m$^3$. The density step size is 10 kg/m$^3$. The sulfur content of the core is assumed to be between 0% and 14%, varied with a step size of 1%. Limiting the range to a value below 15% means that during core solidification the sulfur remains in the liquid phase. The silicon content of the core is varied between 0% and 26% with a step size of 2%, a range comparable to the values used in previous work (Hauck et al., 2013; Knibbe & van Westrenen, 2015). The temperature at the CMB is initially assumed to be between 1400 K for a cold mantle and 2000 K representing a very hot mantle. The step size is 10 K. Note, however, that the most likely range might be between 1600 and 1850 K based on the liquidus of the mantle and the thermal evolution models (e.g., Tosi et al., 2013). By choosing a more conservative temperature range, we compensate for other uncertainties, for example, the unknown crustal enrichment factor.

Each node of the input parameters grid is then combined with a node of the observables grid, which corresponds to the mean density ($\rho$), the mean MoI, and the fractional part of the MoI of the mantle ($C_m/C$). The used mean MoI is 0.346 $\pm$ 0.014 and has been taken from Margot et al. (2012) but is consistent with the value derived by Stark et al. (2015). The assumed $C_m/C$ value is 0.421 $\pm$ 0.025 and taken from Stark et al. (2015). However, within the used error intervals the $C_m/C$ is also consistent with the value 0.431 $\pm$ 0.021 determined by Margot et al. (2012). The MoI and $C_m/C$ are varied within their 3-$\sigma$ error bar with a step size of 0.02. We thereby obtain around 166 million possible combinations of initial parameter sets equally distributed within the parameter space. The remaining unknowns of the model are the radius of the core ($R_c$), its density parameterized by the reference density ($\rho_0$) via equation (1), and the density of the mantle ($\rho_m$). For each grid point of the observables and initial model parameters, we solve for $R_c$, $\rho_0$, $\rho_m$ by iteratively modifying their values using the Levenberg-Marquardt algorithm (Levenberg, 1944; Marquardt, 1963). In details, a first guess is used to compute the pressure at the CMB. Note that the mantle density is kept constant for all sublayers. Using the core modeling described above, we then determine the core size. The resulting density profile is used to compute the geodetic observables ($C/MR^2$, $C_m/C$, $\rho$), which are then compared to the values of the current node of the observables grid. The iteration is stopped when the target values for the MoI and $C_m/C$ is reached with a relative accuracy better than $10^{-6}$ and the mean density is within the error bounds.

The numerical procedure just described does not guarantee that density is always increasing with depth. A solution is retained only if the resulting model is hydrostatic and if the solved core reference density is consistent with laboratory measurements as listed in Table 1 within $\pm$200 kg/m$^3$ for the respective composition of the model. The $\pm$200 kg/m$^3$ is an upper bound on the individual laboratory measurement errors on the reference densities. After applying these constraints, we have around 1.3 million models left.

An example model is given in Figure 1. The pressure for this model is around 6 GPa at the CMB and 36 GPa in the center, in agreement with previous studies (Dumberry & Rivoldini, 2015; Hauck et al., 2013).

### 2.3. Rheological Models

In a second step the rheological model is computed. For this step we follow the same approach as Padovan et al. (2014) using a Maxwell model for the inner and outer core and crust and a pseudo-period Andrade model for the mantle (Jackson & Faul, 2010). Each valid structural model is provided with a set of different mantle rheologies, parameterized by the unrelaxed rigidity and the grain size. For the unrelaxed rigidity, we use values between 59 and 71 GPa and a step size of 2 GPa based on mineralogical models for the mantle of Mercury (Malavergne et al., 2010; Padovan et al., 2014; Rivoldini et al., 2009). The grain size is varied between 1 mm and 1.2 cm with a step size of 2 mm. Based on these, the tidal Love number $k_2$ is calculated and compared against the measurement. The nominal value used for $k_2$ is 0.464 $\pm$ 0.023 (Verma & Margot, 2016) but the 3-$\sigma$ error bar includes the value determined by Mazarico et al. (2014). Since Mercury has a thin mantle which does not reach high pressures, the effect of compressibility can be neglected. The tidal Love numbers can then be computed using a matrix propagation method (e.g., Segatz et al., 1988) taking as input the radial profile of density and complex shear modulus $\mu$, which in the case of a Maxwell model is given by

$$\mu = \frac{i\omega\mu_U}{i\omega + \frac{\mu_U}{\eta}}. \tag{11}$$

In equation (11) $\omega$ is the tidal frequency $2\pi/t$ with $t$ being the tidal period, that is, ≈88 days for Mercury (Van Hoolst & Jacobs, 2003). $\mu_U$ is the unrelaxed rigidity of the corresponding layer and $\eta$ its viscosity. The ratio $\eta/\mu_U$ corresponds to the Maxwell-time $\tau_M$ of the material. In the case where $\tau_M \gg 2\pi/\omega$ the medium reacts

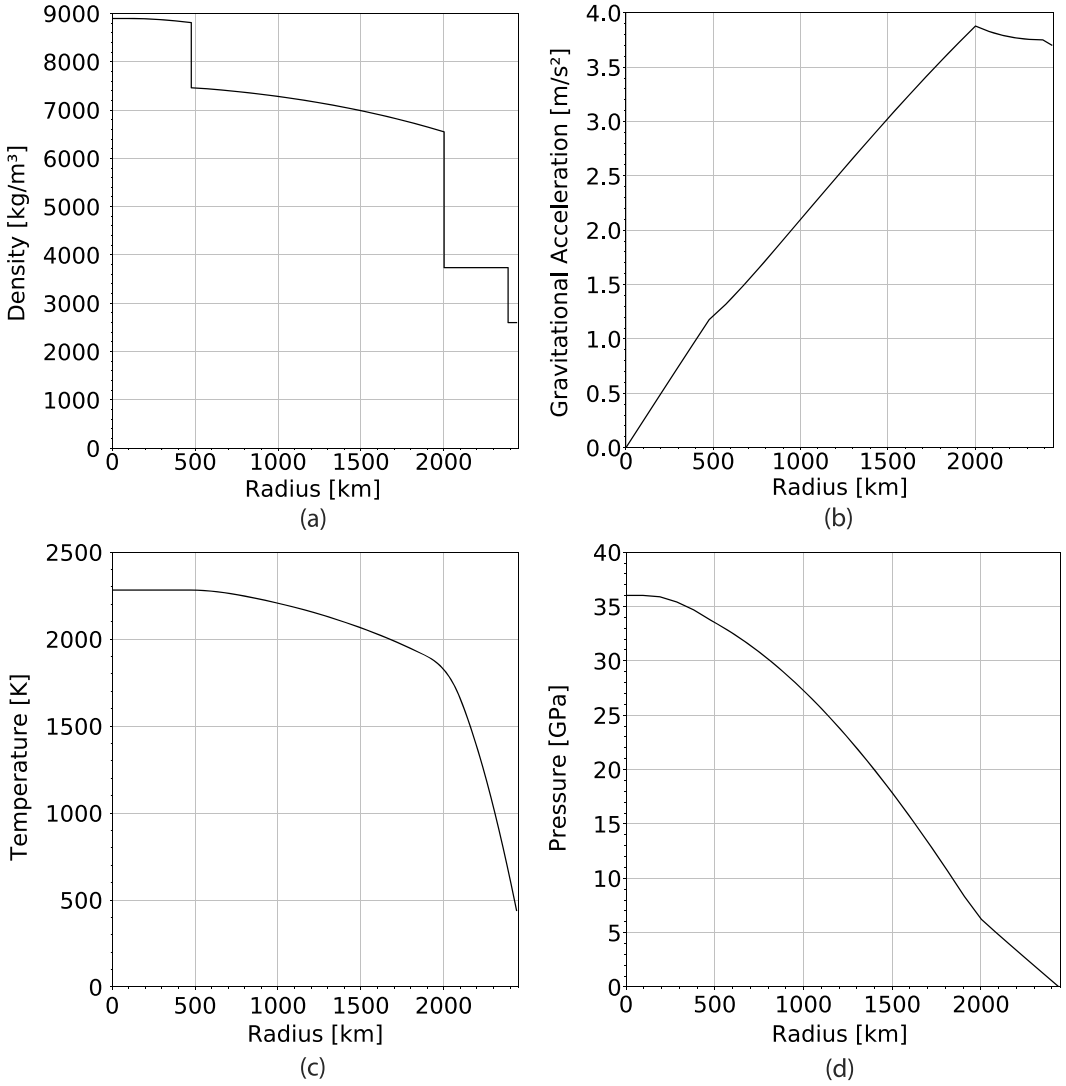


**Figure 1.** Example of a structural model consistent with the geodetic constraints. The core has 6 wt% sulfur, 8 wt% silicon, and a radius of about 2,000 km. Panel (a) shows the density profile assumed constant in the mantle and the crust. The phase transition from a liquid to solid core occurs at a radius of around 500 km. Panel (b) shows the gravitational acceleration and Panels (c) and (d) show the temperature and pressure profiles. The pressure is around 6 GPa at the core-mantle boundary and 36 GPa in the center.

fully elastically to external forces, while in the case $\tau_M \ll 2\pi/\omega$ the material is in the fluid regime. We use the Maxwell rheology for the solid inner core and the crust since both are assumed to respond elastically and the liquid core is in the fluid regime. However, the mantle is expected to show a viscoelastic response to the external tidal potential ($\tau_M \approx 2\pi/\omega$) and it has been shown previously that in this case a Maxwell description is inadequate since it does not provide a good fit to laboratory and field data in the low-frequency range (Efroimsky & Lainey, 2007; Nimmo et al., 2012; Padovan et al., 2014). Therefore, for the mantle we employ the Andrade pseudo-period model introduced by Jackson and Faul (2010), which has been fitted against melt-free olivine. Even if the Andrade model has been successfully applied for a wide set of materials, it should nonetheless be noted that the application to tidal frequencies is still an extrapolation. The complex shear modulus within this model is expressed as

$$\mu = \frac{1}{J_R - iJ_I}, \tag{12}$$

where $J_R$ and $J_I$ are the real and negative imaginary parts of the complex compliance given as

$$J_R = \frac{1}{\mu_U}\left[1 + \beta^*\Gamma(1+\alpha)\omega_p^{-\alpha}\cos\left(\frac{\alpha\pi}{2}\right)\right], \tag{13}$$

$$J_I = \frac{1}{\mu_U}\left[\beta^*\Gamma(1+\alpha)\omega_p^{-\alpha}\sin\left(\frac{\alpha\pi}{2}\right) + \frac{1}{\omega_p\tau_M}\right]. \tag{14}$$

In the equations above, $\mu_U$ denotes the unrelaxed rigidity, $\alpha$ and $\beta^*$ are the Andrade creep coefficient and parameter, respectively, and $\Gamma$ is the Gamma-function. The tidal frequency is replaced here by the pseudo-frequency $\omega_p = 2\pi/X_b$, where $X_b$ is the pseudo-period master variable (Jackson & Faul, 2010; Padovan et al., 2014). It is temperature- and pressure-dependent and can be computed by

$$X_b = T_0\left(\frac{d}{d_R}\right)^{-m}\exp\left[\left(\frac{-E_B}{R}\right)\left(\frac{1}{T}-\frac{1}{T_R}\right)\right]\exp\left[\left(\frac{-V}{R}\right)\left(\frac{P}{T}-\frac{P_R}{T_R}\right)\right]. \tag{15}$$

The exponent $m$ characterizes the dependence on the grain size $d$. $E_B$ is the activation energy and $V$ the activation volume. $R$ is the ideal gas constant and $P_R$ and $T_R$ are the reference temperature and pressure. The unrelaxed rigidity can be calculated from the temperature and pressure of the respective layer. We calculate them for a reference temperature of $T_R$ = 1173 K and a reference pressure of $P_R$ = 0.2 GPa (Jackson & Faul, 2010) as

$$\mu_U(T_R, P_R) = \mu_0 + (T - T_R)\frac{d\mu}{dT} + (P - P_R)\frac{d\mu}{dP}. \tag{16}$$

For the composite rigidity $\mu_0$, we used values between 59 and 71 GPa representing the possible end members of Mercury's mantle composition calculated by Padovan et al. (2014) based on mineralogical models by Rivoldini et al. (2009) and Malavergne et al. (2010). $d\mu/dT$ is set to $13.6 \times 10^{-3}$ GPa/K and $d\mu/dP$ to 1.8 (Jackson & Faul, 2010). We consider grain sizes are between 0.5 and 1.2 cm. This range covers values expected from creep mechanisms in the mantle (e.g., Karato & Wu, 1993) and the preferred values for the grain size of Mars and the Moon (Nimmo et al., 2012; Nimmo & Faul, 2013). All further parameters used to compute the rheology in this study are summarized in Table 2. The pressure inside each layer is given by the respective structural model and the temperature is controlled by the CMB temperature as well as by the surface temperature, which is set to 440 K (Padovan et al., 2014). The temperature profile is obtained by solving the static heat conduction equation

$$k\frac{1}{r^2}\frac{d}{dr}\left(r^2\frac{dT}{dr}\right) + \rho H = 0. \tag{17}$$

The heat production rate $H$ is set for the crust to $H_c = 2.2 \times 10^{-11}$ W/kg (Peplowski et al., 2011). For the mantle we used $H_m = H_c/2.5$ (Padovan et al., 2014) in agreement with the enrichment factor derived by Tosi et al. (2013). The value of the thermal conductivity $k$ is set to 3.3 W/m/K (e.g., Tang et al., 2014). For a given temperature profile the rigidity and viscosity of each layer can then be derived from the complex compliance by

$$\mu = 1/\sqrt{\left|J_R^2 + J_I^2\right|}, \tag{18}$$

$$\eta = 1/(J_I\omega_p). \tag{19}$$

## 3. Results

We find models with liquid cores between 1,950 and 2,100 km in agreement with Hauck et al. (2013), Rivoldini and Van Hoolst (2013), and Knibbe and van Westrenen (2015). Mantle densities are between 2,800 and 4,000 kg/m$^3$, a range that covers all possible composition models for Mercury's mantle (e.g., Padovan et al., 2014; Rivoldini et al., 2009). The maximum inner core size is around 1,500 km, which is compliant with the models found by Dumberry and Rivoldini (2015) but slightly smaller than 1,690 km found by (Knibbe & van Westrenen, 2015). However, this is likely related to the parameter spaces used in the individual studies. We do not have any models without light-alloying elements in the core. Any of these models would freeze out and a completely solid core is not in agreement with the geodetic constraints.

**Table 2**
*Rheological Parameters Used in the Computation of the Tidal Love Numbers*

| Parameter | Symbol | Value | Unit | Reference |
|---|---|---|---|---|
| Crust rigidity | $\mu_U$ | 55 | GPa | Padovan et al. (2014) |
| Crust viscosity | $\eta$ | $10^{23}$ | Pa/s | Padovan et al. (2014) |
| Liquid core rigidity | $\mu_U$ | 0 | GPa | - |
| Liquid core viscosity | $\eta$ | 0 | GPa | - |
| Solid core rigidity | $\mu_U$ | 100 | GPa | Padovan et al. (2014) |
| Solid core viscosity | $\eta$ | $10^{20}$ | Pa/s | Padovan et al. (2014) |
| Andrade creep coefficient | $\alpha$ | 0.33 | - | Jackson and Faul (2010) |
| Andrade creep parameter | $\beta$ | 0.02 | - | Jackson and Faul (2010) |
| Reference temperature | $T_R$ | 1173 | K | Jackson and Faul (2010) |
| Reference pressure | $P_R$ | 0.2 | GPa | Jackson and Faul (2010) |
| Reference grain size | $d_R$ | 3.1 | $\mu$m | Jackson and Faul (2010) |
| Grain size exponent | $m$ | 1.31 | - | Jackson and Faul (2010) |
| Activation volume | $V$ | $10^{-5}$ | $m^3$/mol | Jackson and Faul (2010) |
| Activation energy | $E_B$ | 303 | kJ/mol | Jackson and Faul (2010) |

### 3.1. Tidal Love Numbers

Typical $k_2$ values range between 0.45 and 0.52 implying that the measured value argues for a high mantle rigidity, large grain sizes, and/or a lower temperature at the CMB in agreement with Padovan et al. (2014). In the considered range of models the tidal Love number $h_2$ ranges between 0.77 and 0.93. The corresponding radial tidal amplitudes are between 1.93 and 2.33 m at the equator and 0.24 and 0.29 m at the poles. For the tidal Love number $l_2$, we find values between 0.17 and 0.20. The main parameters controlling $h_2$ are the size of the liquid core and the unrelaxed rigidity of the mantle, while the sensitivity to the mantle density is small. Both CMB temperature and grain size influence $h_2$ (section 3.3) through their strong effects on viscosity (equation (15)).

### 3.2. Inner Core Radius

The size of Mercury's inner core is a key parameter to understand the workings of the planetary dynamo. Previous studies (Dumberry & Rivoldini, 2015) found that the radius of the inner core is likely smaller than ≈ 1,300 km with smaller core sizes being favored, while Knibbe and van Westrenen (2015) found a maximum inner core size of 1,690 km. However, no direct measurements are currently available and it is not evident that an improved measurement accuracy of the MoI and $C_m/C$ will lead to a direct detection (Margot et al., 2017; Rivoldini & Van Hoolst, 2013). Peale et al. (2016) pointed out that the value of the MoI has to be adjusted due to a possible additional torque from a nonspherical inner core. This effect is greater for larger inner core radii (>35% of the solid core radius). For smaller inner core radii, the MoI would not be affected significantly. In the most extreme case (large and dense inner core) with an inner core radius and density of 60% of the outer core radius and 10,000 kg/$m^3$, respectively, the dimensionless MoI would be reduced to about 0.316. Furthermore, Dumberry et al. (2013) showed that the 88 days libration amplitude has to be corrected by a factor of $1/(1+\zeta)$ where $\zeta$ can reach values of order 0.05 for large inner cores, resulting in an overestimation of $C_m/C$ by up to 5%. Both effects show the importance of attempting to place constraints on the inner core size. These possible reductions have to be taken into account when placing the constraints on our models. In this study we use the constraints from the MoI without taking additional torques from the inner core into account. Should the values obtained for $h_2$ suggest a large, dense inner core, the MoI constraints would have to be adjusted accordingly.

The measurement of $h_2$ is listed among the objectives of the BepiColombo Laser Altimeter (BELA) aboard the BepiColombo mission (Thomas et al., 2007). An important advantage of having both tidal Love numbers is that certain trade-offs among the parameters can be suppressed by combining them (e.g., Hussmann et al., 2011; Wahr et al., 2006). The main parameter controlling the magnitude of $k_2$ and $h_2$ in case of Mercury is the radius of the liquid part of the core. Further, the amplitude of the tidal deformation is controlled by the mantle rheology. For the given geodetic constraints, and for each Love number individually, the magnitude is mainly controlled by the thickness and rheological properties of the mantle, while the size of the inner core

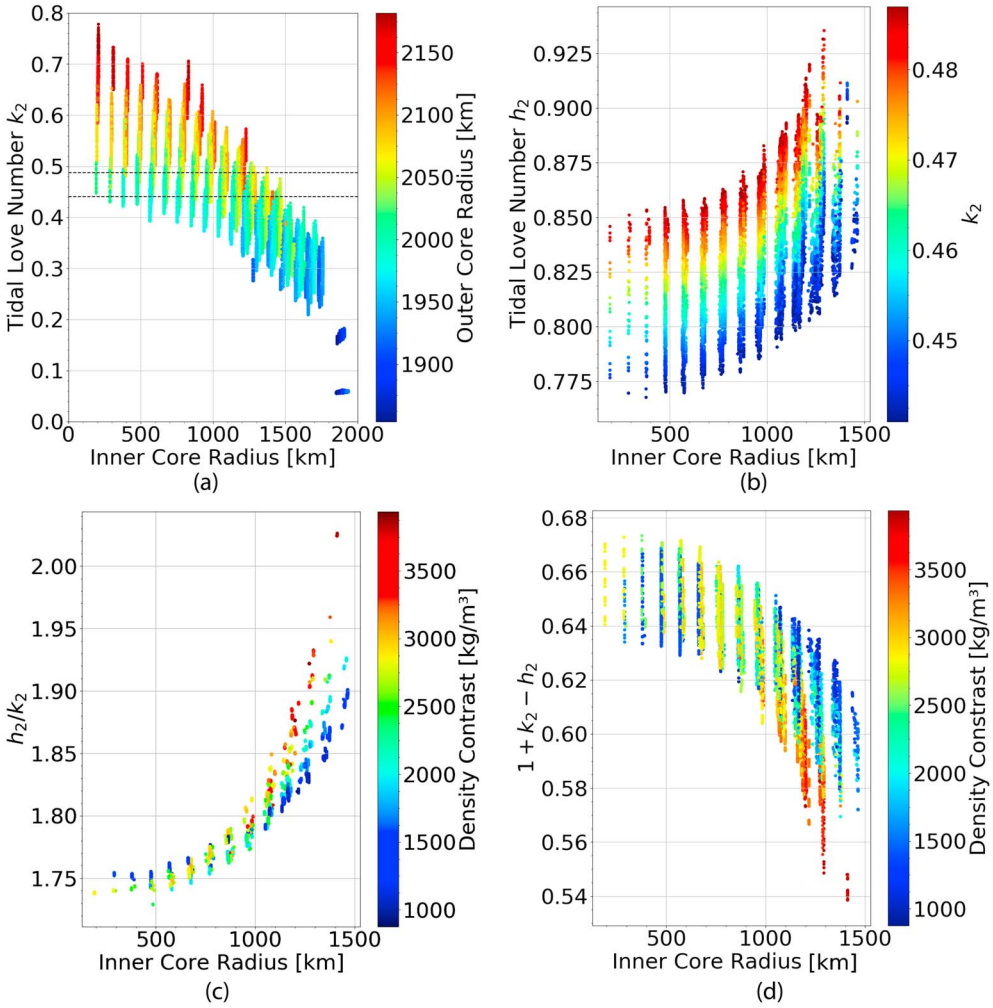


**Figure 2.** (a) Tidal Love number $k_2$ as a function of inner core size for the full range of models consistent with the geodetic constraints. No useful inferences can be made from the measured $k_2$ range (dashed lines). (b) The tidal Love number $h_2$ for the subset of models in agreement with the $k_2$ error interval from panel (a). The observable trend is given by the strong correlation with $k_2$. (c) $h_2/k_2$ as a function of inner core size. The distribution of points is relatively tight and therefore potentially useful to constrain the inner core size. (d) The diminishing factor $1 + k_2 - h_2$ as a function of the inner core size. As for $h_2/k_2$ in panel (c), there is a clear trend, however it provides a less strict constraint.

has only a minor influence (Figure 2a). However, a linear combination as well as the ratio $h_2/k_2$ cancels out the ambiguity to a certain extent. In presence of a density contrast between a solid core and a liquid core, the size of an inner core is noticeable when combining both Love numbers. It should be noted that the density contrast alone is not sufficient to observe the effect, the inner core must be solid, that is, in a predominantly elastic regime ($\tau_M > 2\pi/\omega$). Two liquid core layers with a strong density contrast would not reproduce the same effect. Thus, an inner core showing a fluid response might not be revealed with the method proposed here or it would appear to be smaller than its actual size, if the fluid response characterize only the outer part of the inner core. The effect is further not limited to the measured value of $k_2$ but also noticeable when assuming the full range of models from Figure 2a. The linear combination $1 + k_2 - h_2$, known as the *diminishing factor*, has been proposed previously to better constrain thickness of the outer ice layer of Jupiter's moon Europa (Wahr et al., 2006) and of other icy satellites as Ganymede (Steinbrügge et al., 2015). The diminishing factor decreases with increasing inner core size, and the trend is stronger for larger inner cores. Similarly, the ratio $h_2/k_2$ increases with increasing inner core size, in particular for the larger sizes. The distribution of data points is tighter for the ratio $h_2/k_2$ than for the diminishing factor (Figures 2c and 2d). This finding implies that with an accurate $h_2$ determination, a measure of $h_2/k_2$ could provide at least an upper bound on the inner core

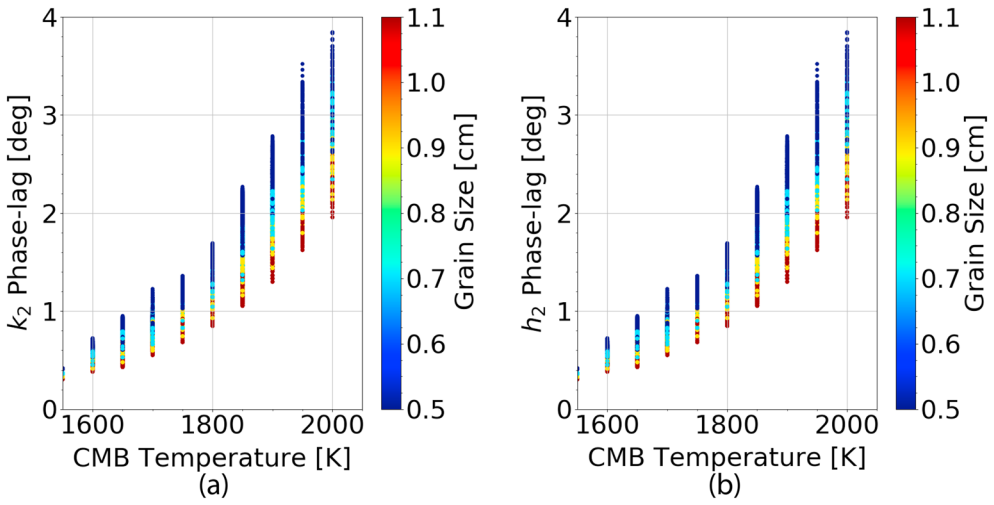


**Figure 3.** Phase-lag of (a) $k_2$ and (b) $h_2$ as a function of the temperature at the CMB. The difference between both phase-lags is < 0.2 at maximum and therefore barely noticeable. CMB = core-mantle boundary.

size. For inner cores larger than about 700 km, the steep slope of the $h_2/k_2$ versus inner core size distribution implies that the inner core size could potentially be inferred to roughly ±100 km.

### 3.3. Phase-lags

The tidal Love numbers are complex numbers that are characterized by their amplitude and phase, which are a function of the rheological parameters. The tidal phase-lag is defined as

$$\arctan(\varphi_{k2}) = \frac{\mathrm{Im}(k_2)}{\mathrm{Re}(k_2)}. \tag{20}$$

$\mathrm{Re}(k_2)$ and $\mathrm{Im}(k_2)$ are the real and imaginary part of the complex number $k_2$, respectively. In the elastic and fluid limit of the rheology, the Maxwell-time is either significantly larger or lower than the forcing period, in which case the body reacts instantly to the tidal forcing. Such a case implies further that no heat is dissipated. The more the forcing period approaches the Maxwell-time, the more the body reacts viscoelastically and the more heat is dissipated. The tidal dissipation can be derived from a multipole expansion in eccentricity and inclination. To zero-th order inclination and fourth order in eccentricity $e$ the mean tidal dissipation rate can be derived from Makarov and Efroimsky (2014) as

$$\dot{E} = \frac{GM_{\mathrm{Sun}}^2 R^5 n}{a^6}\mathrm{Im}(k_2)\left(\frac{3}{4} - \frac{39}{16}e^2 + \frac{2043}{32}e^4\right), \tag{21}$$

with $R$, $a$, and $n$ being Mercury's radius, semi-major axis, and mean motion, respectively. $GM_{\mathrm{Sun}}$ is the gravitational parameter of the Sun. A particularity of the 3:2 resonance is that the tidal dissipation barely depends on the eccentricity. Therefore, also a body with a significant eccentricity like Mercury does not dissipate much tidal energy. The main source of tidal dissipation on Mercury is the mantle and the maximum values for $\mathrm{Im}(k_2)$ consistent with the geodetic constraints range between 0.02 and 0.03 corresponding to a phase-lag of less than 4° (Figure 3). This result is consistent with the maximum value derived by Baland et al. (2017) estimated from the spin orientation. The maximum tidal dissipation expected from equation (21) using $e = 0.205$, $a = 57.9 \times 10^6$ km, and an orbital period of 88 days corresponds to a surface heat flux <0.16 mW/m$^2$. Figure 3 shows the same range for the phase-lags of $h_2$ and $k_2$. This is in contrast to the case of icy satellites, where the phase-lag difference can be indicative for dissipation in the deep interior (Hussmann et al., 2016). The maximum difference is expected to be 0.2° but due to the small radial amplitudes the phase-lag of $k_2$ is more likely to be measured than the $h_2$-lag (see section 4). Using a viscoelastic inner core instead could lead to a phase-lag difference of up to 0.8°. Since the compliance is mainly controlled by the temperature and grain size, a measurement of a tidal phase-lag with an accuracy better than 0.5° would however help to further constrain the temperature at the CMB and the grain size and therefore also further constrain the physical state of the core. It should be noted, however, that the exact value of the phase-lag and corresponding dissipation depends on the rheological model. We adopted the Andrade pseudo-period model, which is based on olivine (Jackson &

Faul, 2010). While the dominant mineral in Mercury's mantle may indeed be olivine (Namur et al., 2016; Vander Kaaden & McCubbin, 2016), it is certainly not the only mineral. Furthermore, the iron content of Mercury's mantle is unknown, and iron has a strong influence on the flow properties of olivine (Zhao et al., 2009). However, our approach is warranted given that the simple Maxwell model is not able to fit observational and field data (e.g., Efroimsky & Lainey, 2007) and that the Andrade pseudo-period depends on a smaller number of unknown parameters with respect to the possibly superior extended Burgers-model (Jackson & Faul, 2010).

## 4. Discussion and Conclusion

We constructed a broad range of Mercury interior models compliant with MESSENGER measurements of mean density, MoI, and $C_m/C$ within their 3-$\sigma$ range. Our approach to sample the parameter space in a regular grid is chosen to ensure that the complete range of possible models in agreement with the measurement constraints are represented in our analysis. If our current understanding of the interior structure of Mercury is correct, then a measurement of the tidal Love number $h_2$ should fall within the range from 0.77 to 0.93. The corresponding peak-to-peak deformations are between 1.93 and 2.33 m at the equator and between 0.24 and 0.29 m at the poles. These values are based on conservative ranges for the model parameters. Refined measurements of the MoI, $C_m/C$, and $k_2$ are therefore expected to further constrain the range of radial surface deformations. The remaining uncertainties should mainly be captured inside the interior modeling. Despite different values for the parameters listed in Table 1 have been used previously in the literature, varying the parameters involved shows that the results for the tides we presented in this study are robust against reasonable variations on those parameters. Our models do not account for possible iron snow regimes, which might result in a thermal boundary layer in the upper core. However, such a boundary layer would have minor impact on the tidal Love numbers as long as the core is partially liquid. While for the most part the model parameters rely on laboratory measurements, uncertainties mainly linked to the composition of the core remain and a measured $h_2$ number outside the predicted range could point out inaccurate assumptions of present-day interior models. In the case of a compliant measurement the remaining range of possible values is particularly valuable to obtain additional constraints on the inner core size. Circumstantial evidence points toward a small inner core, that is, <1,000 km in radius (e.g., Margot et al., 2017). This assumption could be confirmed or rejected with the proposed $h_2/k_2$ measurement. In case of a small inner core however, its size is unlikely to be constrained due to the little sensitivity of $h_2/k_2$ to a small inner cores (Figure 2c). In case of an inner core with a radius above 1,000 km, its size could be constrained due to the rapid growth of the $h_2$ over $k_2$ ratio. Therefore, it would also allow for reassessing the MoI and providing constraints for models addressing Mercury's core dynamics and related magnetic field generation. It is important to note that the dependence of the ratio $h_2/k_2$ on the radius of the inner core is independent of the assumed rheological model since the same results hold when using a simple Maxwell rheological model for the mantle (see supporting information). Taking advantage of the $h_2/k_2$ versus inner core size dependence requires that the tidal Love number $h_2$ can be measured with sufficient accuracy. Assuming that the $h_2$ determination dominates the $h_2/k_2$ error budget at the upcoming BepiColombo mission, an absolute accuracy of $< 0.05$ in $h_2$ would be needed to discriminate between a large and a small core. For an $h_2$ value of 0.8 this corresponds to a measurement error of 6%. This is close to the estimated 7% by Koch et al. (2010) for the BELA (Thomas et al., 2007). The authors suggest inferring $h_2$ from the time dependency of the spherical harmonics expansion of Mercury's topography. However, their estimation assumes a mission life time of 4 years and does not treat a wide range of systematic errors (e.g., instrument alignment or rotational state). Indeed, due to the low tidal amplitudes and the 10 Hz shot frequency of BELA, an accurate-enough determination will be very challenging. Alternative methods like cross-over measurements suffer from the low-rotation rate of Mercury and a consequently low amount of cross-over points at lower latitudes during the nominal mission (Steinbrügge et al., 2018). Therefore, current estimates of the $h_2$ measurement accuracies point toward a confirmation or rejection of the presence of a large inner core. However, a further assessment of the size of the inner core will depend on the final instrument performance in orbit, the mission lifetime, the accuracy of the alignment calibration, as well as on the quality of the orbit reconstruction.

The tidal phase-lag is inferred to be lower than 4°. The tidal dissipation would then correspond to a surface heat flux of <0.16 mW/m$^2$. A measurement of the tidal phase-lag can be used to constrain the temperature at the CMB for a given grain size and under the condition that the profile is conductive, which seems to be the case based on thermal evolution models (Padovan et al., 2017; Tosi et al., 2013), and thereby further constrain the physical state of Mercury's core. The accuracy on the real and imaginary part of $k_2$ has been estimated for

the Mercury Orbiter Radio Experiment (Iess et al., 2009) on board of the upcoming BepiColombo mission to be $2.6 \times 10^{-4}$ (Imperi et al., 2018). This corresponds to a phase-lag measurement with an accuracy of <0.1° and therefore provides the needed precision. An estimate for the $h_2$ phase-lag is currently not available, due to the small expected radial amplitudes unlikely to be measured. We expect it to be very similar to the $k_2$-lag and below 4°. Therefore, refined measurements of Mercury's gravity field and librations together with a simultaneous determination of $h_2$ as well as both the real and imaginary part of $k_2$ by the upcoming mission can constrain the interior structure of Mercury, including the inner core size and possibly the temperature profile, to an unprecedented level.

**Acknowledgments**
The authors would like to thank Frank Sohl, Tina Rückriemen-Bez, and Doris Breuer for helpful discussions and Mathieu Dumberry and an anonymous reviewer for their comments that greatly improved the content and clarity of this manuscript. S. Padovan was supported by the DFG within the research Unit FOR 2440 *Matter Under Planetary Interior Conditions*. A. Stark was supported by a research grant from the Helmholtz Association and German Aerospace Center (DLR). All data for this paper are properly cited and referred to in the reference list. The numerical output necessary to generate the figures is given in the supplementary data. This is UTIG contribution 3283.

## References

Anderson, B. J., Johnson, C. L., Korth, H., Winslow, R. M., Borovsky, J. E., Purucker, M. E., et al. (2012). Low-degree structure in Mercury's planetary magnetic field. *Journal of Geophysical Research*, *117*, E00L12. https://doi.org/10.1029/2012JE004159

Baland, R. M., Yseboodt, M., Rivoldini, A., & Hoolst, T. V. (2017). Obliquity of Mercury: Influence of the precession of the pericenter and of tides. *Icarus*, *291*, 136–159. https://doi.org/10.1016/j.icarus.2017.03.020

Benkhoff, J., van Casteren, J., Hayakawa, H., Fujimoto, M., Laakso, H., Novara, M., et al. (2010). Bepicolombo—comprehensive exploration of mercury: Mission overview and science goals. *Planetary and Space Science*, *58*(1-2), 2–20. https://doi.org/10.1016/j.pss.2009.09.020

Beutl, M., Pottlacher, G., & Jäger, H. (1994). Thermophysical properties of liquid iron. *International Journal of Thermophysics*, *15*(6), 1323–1331. https://doi.org/10.1007/BF01458840

Cao, H., Aurnou, J. M., Wicht, J., Dietrich, W., Soderlund, K. M., & Russell, C. T. (2014). A dynamo explanation for Mercury's anomalous magnetic field. *Geophysical Review Letters*, *41*, 4127–4134. https://doi.org/10.1002/2014GL060196

Dumberry, M., & Rivoldini, A. (2015). Mercury's inner core size and core-crystallization regime. *Icarus*, *248*, 254–268. https://doi.org/10.1016/j.icarus.2014.10.038

Dumberry, M., Rivoldini, A., Van Hoolst, T., & Ysebodt, M. (2013). The role of Mercury's core density structure on its longitudinal librations. *Icarus*, *225*, 62–74. https://doi.org/10.1016/j.icarus.2013.03.001

Efroimsky, M., & Lainey, V. (2007). Physics of bodily tides in terrestrial planets and the appropriate scales of dynamical evolution. *Journal of Geophysical Research*, *112*, E12003. https://doi.org/10.1029/2007JE002908

Hauck, S. A., Margot, J. L., Solomon, S. C., Phillips, R. J., Johnson, C. L., Lemoine, F. G., et al. (2013). The curious case of Mercury's internal structure. *Journal of Geophysical Research: Planets*, *118*, 1204–1220. https://doi.org/10.1002/jgre.20091

Hauck, S. A., Solomon, S. C., & Smith, D. A. (2007). Predicted recovery of Mercury's internal structure by MESSENGER. *Geophysical Research Letters*, *34*, L18201. https://doi.org/10.1029/2007GL030793

Hussmann, H., Shoji, D., Steinbrügge, G., Stark, A., & Sohl, F. (2016). Constraints on dissipation in the deep interiors of Ganymede and Europa from tidal phase-lags. *Celestial Mechanics and Dynamical Astronomy*, *126*(1), 131–144. https://doi.org/10.1007/s10569-016-9721-0

Hussmann, H., Sohl, F., & Oberst, J. (2011). Measuring tidal deformations at Europa's surface. *Advances in Space Research*, *48*, 718–724. https://doi.org/10.1016/j.asr.2010.06.001

Iess, L., Asmar, S., & Tortora, P. (2009). MORE: An advanced tracking experiment for the exploration of Mercury with the mission BepiColombo. *Acta Astronautica*, *65*(5), 666–675. https://doi.org/10.1016/j.actaastro.2009.01.049

Imperi, L., Iess, L., & Mariani, M. J. (2018). An analysis of the geodesy and relativity experiments of BepiColombo. *Icarus*, *301*, 9–25. https://doi.org/10.1016/j.icarus.2017.09.008

Jackson, I., & Faul, U. H. (2010). Grainsize-sensitive viscoelastic relaxation in olivine: Towards a robust laboratory-based model for seismological application. *Physics of the Earth and Planetary Interiors*, *183*(1), 151–163. https://doi.org/10.1016/j.pepi.2010.09.005

Jing, Z., Wang, Y., Kono, Y., Yu, T., Sakamaki, T., Park, C., et al. (2014). Sound velocity of Fe-S liquids at high pressure: Implications for the Moon's molten outer core. *Earth and Planetary Science Letters*, *396*, 78–87. https://doi.org/10.1016/j.epsl.2014.04.015

Karato, S.-I., & Wu, P. (1993). Rheology of the upper mantle: A synthesis. *Science*, *260*, 771–778. https://doi.org/10.1126/science.260.5109.771

Knibbe, J. S., & van Westrenen, W. (2015). The interior configuration of planet Mercury constrained by moment of inertia and planetary contraction. *Journal of Geophysical Research: Planets*, *120*, 1904–1923. https://doi.org/10.1002/2015JE004908

Koch, C., Kallenbach, R., & Christensen, U. (2010). Mercury's global topography and tidal signal from laser altimetry by using a rectangular grid. *Planetary and Space Science*, *58*(14), 2022–2030. https://doi.org/10.1016/j.pss.2010.10.002

Komabayashi, T., & Fei, Y. (2010). Internally consistent thermodynamic database for iron to the Earth's core conditions. *Journal of Geophysical Research*, *115*, B03202. https://doi.org/10.1029/2009JB006442

Kuwayama, Y., & Hirose, K. (2004). Phase relations in the system Fe-FeSi at 21 GPa. *American Mineralogist*, *89*(2-3), 273–276. https://doi.org/10.2138/am-2004-2-303

Levenberg, K. (1944). A method for the solution of certain problems in least squares. *Quarterly of Applied Mathematics*, *2*(2), 164–168. https://doi.org/10.1137/0111030

Lin, J. F., Campbell, A. J., Heinz, D. L., & Shen, G. (2003). Static compression of iron-silicon alloys: Implications for silicon in the Earth's core. *Journal of Geophysical Research*, *108*(B1), 2045. https://doi.org/10.1029/2002JB001978

Makarov, V., & Efroimsky, M. (2014). Tidal dissipation in a homogeneous spherical body. II. Three examples: Mercury, IO, and Kepler-10 b. *The Astrophysical Journal*, *795*, 7. https://doi.org/10.1088/0004-637X/795/1/7

Malavergne, V., Toplis, M. J., Berthet, S., & Jones, J. (2010). Highly reducing conditions during core formation on Mercury: Implications for internal structure and the origin of a magnetic field. *Icarus*, *206*, 199–209. https://doi.org/10.1016/j.icarus.2009.09.001

Manglik, A., Wicht, J., & Christensen, U. R. (2010). A dynamo model with double diffusive convection for Mercury's core. *Earth and Planetary Science Letters*, *289*(3), 619–628. https://doi.org/10.1016/j.epsl.2009.12.007

Margot, J. L., Hauk, S. A. II, Mazarico, E., Padovan, S., & Pealo, S. J. (2017). Mercury's internal structure. In S. Solomon, et al. (Eds.), *Mercury - The view after MESSENGER*. Cambridge: Cambridge University Press.

Margot, J. L., Peale, S., Jurgens, R., Slade, M., & Holin, I. (2007). Large longitude libration of Mercury reveals a molten core. *Science*, *316*, 710–714. https://doi.org/10.1126/science.1140514

Margot, J. L., Peale, S. J., Solomon, S. C., Hauck, S. A., Ghigo, F. D., Jurgens, R. F., et al. (2012). Mercury's moment of inertia from spin and gravity data. *Journal of Geophysical Research*, *117*, E00L09. https://doi.org/10.1029/2012JE004161

Marquardt, D. W. (1963). An algorithm for least-squares estimation of nonlinear parameters. *Journal of the Society for Industrial and Applied Mathematics*, *11*(2), 431–441. https://doi.org/10.1137/0111030

Mazarico, E., Genova, A., Goossens, S., Lemoine, F. G., Neumann, G. A., Zuber, M. T., et al. (2014). The gravity field, orientation, and ephemeris of Mercury from MESSENGER observations after three years in orbit. *Journal of Geophysical Research: Planets*, *119*, 2417–2436. https://doi.org/10.1002/2014JE004675

Namur, O., Charlier, B., Holtz, F., Cartier, C., & McCammon, C. (2016). Sulfur solubility in reduced mafic silicate melts: Implications for the speciation and distribution of sulfur on Mercury. *Earth and Planetary Science Letters*, *448*, 102–114. https://doi.org/10.1016/j.epsl.2016.05.024

Nimmo, F., & Faul, U. H. (2013). Dissipation at tidal and seismic frequencies in a melt-free, anhydrous Mars. *Journal of Geophysic al Research: Planets*, *118*, 2558–2569. https://doi.org/10.1002/2013JE004499

Nimmo, F., Faul, U. H., & Garnero, E. J. (2012). Dissipation at tidal and seismic frequencies in a melt-free Moon. *Journal of Geophysical Research*, *117*, E09005. https://doi.org/10.1029/2012JE004160

Padovan, S., Margot, J. L., Hauck, S. A., Moore, W. B., & Solomon, S. C. (2014). The tides of Mercury and possible implications for its interior structure. *Journal of Geophysical Research: Planets*, *119*, 850–866. https://doi.org/10.1002/2013JE004459

Padovan, S., Tosi, N., Plesa, A. C., & Ruedas, T. (2017). Impact-induced changes in source depth and volume of magmatism on Mercury and their observational signatures. *Nature Communications*, *8*, 1945. https://doi.org/10.1038/s41467-017-01692-0

Peale, S. J. (1976). Does Mercury have a molten core. *Nature*, *262*, 765–766. https://doi.org/10.1038/262765a0

Peale, S. J., Margot, J. L., Hauck, S. A., & Solomon, S. C. (2016). Consequences of a solid inner core on Mercury's spin configuration. *Icarus*, *264*, 443–455. https://doi.org/10.1016/j.icarus.2015.09.024

Peale, S. J., Phillips, R. J., Solomon, S. C., Smith, D. E., & Zuber, M. T. (2002). A procedure for determining the nature of Mercury's core. *Meteoritics & Planetary Science*, *37*(9), 1269–1283. https://doi.org/10.1111/j.1945-5100.2002.tb00895.x

Peplowski, P. N., Evans, L. G., Hauck, S. A., McCoy, T. J., Boynton, W. V., Gillis-Davis, J. J., et al. (2011). Radioactive elements on Mercury's surface from MESSENGER: Implications for the planet's formation and evolution. *Science*, *333*(6051), 1850–1852. https://doi.org/10.1126/science.1211576

Perry, M. E., Neumann, G. A., Phillips, R. J., Barnouin, O. S., Ernst, C. M., Kahan, D. S., et al. (2015). The low-degree shape of Mercury. *Geophysical Research Letters*, *42*, 6951–6958. https://doi.org/10.1002/2015GL065101

Rivoldini, A., & Van Hoolst, T. (2013). The interior structure of Mercury constrained by the low-degree gravity field and the rotation of Mercury. *Earth and Planetary Science Letters*, *377*, 62–72. https://doi.org/10.1016/j.epsl.2013.07.021

Rivoldini, A., Van Hoolst, T., & Verhoeven, O. (2009). The interior structure of Mercury and its core sulfur content. *Icarus*, *201*, 12–30. https://doi.org/10.1016/j.icarus.2008.12.020

Sanloup, C., Fiquet, G., Gregoryanz, E., Morard, G., & Mezouar, M. (2004). Effect of Si on liquid Fe compressibility: Implications for sound velocity in core materials. *Geophysical Research Letters*, *31*, L07604. https://doi.org/10.1029/2004GL019526

Sanloup, C., Guyot, F., Gillet, P., Fiquet, G., Mezouar, M., & Martinez, I. (2000). Density measurements of liquid Fe-S alloys at high-pressure. *Geophysical Research Letters*, *27*(6), 811–814. https://doi.org/10.1029/1999GL008431

Segatz, M., Spohn, T., Ross, M., & Schubert, G. (1988). Tidal dissipation, surface heat flow, and figure of viscoelastic models of Io. *Icarus*, *75*, 187–206. https://doi.org/10.1016/0019-1035(88)90001-2

Smith, D. E., Zuber, M. T., Phillips, R. J., Solomon, S. C., Hauck, S. A., Lemoine, F. G., et al. (2012). Gravity field and internal structure of Mercury from MESSENGER. *Science*, *336*, 214. https://doi.org/10.1126/science.1218809

Solomon, S. C., McNutt, Jr. R. L., & Prockter, L. M. (2011). Mercury after the MESSENGER flybys: An introduction to the special issue of planetary and space science. *Planetary and Space Science*, *59*(15), 1827–1828.

Stark, A., Oberst, J., Preusker, F., Peale, S. J., Margot, J. L., Phillips, R. J., et al. (2015). First MESSENGER orbital observations of Mercury's librations. *Geophysical Research Letters*, *42*, 7881–7889. https://doi.org/10.1002/2015GL065152

Steinbrügge, G., Stark, A., Hussmann, H., Sohl, F., & Oberst, J. (2015). Measuring tidal deformations by laser altimetry. A performance model for the Ganymede Laser Altimeter. *Planetary and Space Science*, *117*, 184–191. https://doi.org/10.1016/j.pss.2015.06.013

Steinbrügge, G., Stark, A., Hussmann, H., Wickhusen, K., & Oberst, J. (2018). The performance of the BepiColombo Laser Altimeter (BELA) prior launch and prospects for Mercury orbit operations. *Planetary and Space Science*, *159*, 84–92. https://doi.org/10.1016/j.pss.2018.04.017

Tang, X., Ntam, M. C., Dong, J., Rainey, E. S. G., & Kavner, A. (2014). The thermal conductivity of Earth's lower mantle. *Geophysical Research Letters*, *41*, 2746–2752. https://doi.org/10.1002/2014GL059385

Thomas, N., Spohn, T., Barriot, J. P., Benz, W., Beutler, G., Christensen, U., et al. (2007). The BepiColombo Laser Altimeter (BELA): Concept and baseline design. *Planetary and Space Science*, *55*, 1398–1413. https://doi.org/10.1016/j.pss.2007.03.003

Tosi, N., Grott, M., Plesa, A. C., & Breuer, D. (2013). Thermochemical evolution of Mercury's interior. *Journal of Geophysical Research: Planets*, *118*, 2474–2487. https://doi.org/10.1002/jgre.20168

Uchida, T., Wang, Y., Rivers, M. L., & Sutton, S. R. (2001). Stability field and thermal equation of state of $\epsilon$-iron determined by synchrotron X-ray diffraction in a multianvil apparatus. *Journal of Geophysical Research*, *106*(B10), 21,799–21,810. https://doi.org/10.1029/2001JB000258

Van Hoolst, T., & Jacobs, C. (2003). Mercury's tides and interior structure. *Journal of Geophysical Research*, *108*(E11), 5121. https://doi.org/10.1029/2003JE002126

Vander Kaaden, K. E., & McCubbin, F. M. (2016). The origin of boninites on Mercury: An experimental study of the northern volcanic plains lavas. *Geochimica et Cosmochimica Acta*, *173*, 246–263. https://doi.org/10.1016/j.gca.2015.10.016

Verma, A. K., & Margot, J. L. (2016). Mercury's gravity, tides, and spin from MESSENGER radio science data. *Journal of Geophysical Research: Planets*, *121*, 1627–1640. https://doi.org/10.1002/2016JE005037

Wahr, J., Zuber, M., Smith, D., & Luine, J. (2006). Tides on Europa, and the thickness of Europa's icy shell. *Journal of Geophysical Research*, *111*, E12005. https://doi.org/10.1029/2006JE002729

Zhao, Y. H., Zimmerman, M. E., & Kohlstedt, D. L. (2009). Effect of iron content on the creep behavior of olivine: 1. Anhydrous conditions. *Earth and Planetary Science Letters*, *287*, 229–240. https://doi.org/10.1016/j.epsl.2009.08.006